Estimating seismic dispersion from prestack data using frequency-dependent AVO analysis

Xiaoyang Wu[1], Mark Chapman[1,2], Xiang-Yang Li[1]

1 Edinburgh Anisotropy Project, British Geological Survey, Murchison House, West Mains Road, Edinburgh EH9 3LA, UK.

2 School of Geosciences, University of Edinburgh, The King's Buildings, West Mains Road, Edinburgh EH9 3JW, UK.

Abstract

Recent laboratory measurement studies have suggested a growing consensus that fluid saturated rocks can have frequency-dependent properties within the seismic bandwidth. It is appealing to try to use these properties for the discrimination of fluid saturation from seismic data. In this paper, we develop a frequency-dependent AVO (FAVO) attribute to measure magnitude of dispersion from pre-stack data. The scheme essentially extends the Smith and Gidlow (1987)'s two-term AVO approximation to be frequency-dependent, and then linearize the frequency-dependent approximation with Taylor series expansion. The magnitude of dispersion can be estimated with least-square inversion. A high-resolution spectral decomposition method is of vital importance during the implementation of the FAVO attribute calculation. We discuss the resolution of three typical spectral decomposition techniques: the short term Fourier transform (STFT), continuous wavelet transform (CWT) and Wigner-Vill Distribution (WVD) based methods. The smoothed pseudo Wigner-Ville Distribution (SPWVD) method, which uses smooth windows in time and frequency domain to suppress cross-terms, provides higher resolution than that of STFT and CWT. We use SPWVD in the FAVO attribute to calculate the frequency-dependent spectral amplitudes from pre-stack data. We test our attribute on forward models with different time scales and crack densities to understand wave-scatter induced dispersion at the interface between

25 an elastic shale and a dispersive sandstone. The FAVO attribute can determine the maximum magnitude of

26 P-wave dispersion for dispersive partial gas saturation case; higher crack density gives rise to stronger magnitude

27 of P-wave dispersion. Finally, the FAVO attribute was applied to real seismic data from the North Sea. The

28 result suggests the potential of this method for detection of seismic dispersion due to fluid saturation.

29 **Keywords**: frequency dependent AVO; spectral decomposition; prestack; seismic dispersion

30

31

Introduction

Frequency-dependent attenuation and dispersion are attracting more and more interests because they are believed to be directly associated to rock properties such as scale length of heterogeneities, rock permeability and saturating fluid. Theoretical studies of rock physics models (White, 1975; Chapman et al., 2003; Müller and Rothert, 2006; Gurevich et al., 2009) and Laboratory measurements of fluid saturated rocks (Murphy, 1982; Gist, 1994; Quintal and Tisato, 2013) suggested that wave-induced fluid flow between mesoscopic-scale heterogeneities is a major cause of P-wave attenuation and velocity dispersion in partially saturated porous media.

Since seismic attenuation is more sensitive to rock properties than velocity dispersion is, direct Q value estimation and tomography have been widely studied as a seismic attribute for reservoir characterization. The classical spectral ratio (Bath, 1974; Hauge, 1981; Dasgupta and clark, 1998; Taner and Treitel, 2003) utilizes the ratio of seismic amplitude spectra at two different depths varies as a function of frequency to estimate Q value. Central frequency shift method (Quan and Harris, 1997) calculates Q from the decrease in centroid frequency of a spectrum of seismic wave traveling through a lossy medium.

The amplitude-versus-offset (AVO) as a lithology and fluid analysis tool has been utilized for over twenty years. However, the AVO theory is based on Zoeppritz equation and Gassmann's theory, in which attenuation and dispersion is generally not accounted for. Application of spectral decomposition techniques allows the frequency-dependent AVO behavior due to fluid saturation to be detected on seismic data, because reflections from hydrocarbon-saturated zone are thought to have a tendency of being low-frequency (Castagna et al., 2003).

54   Chapman et al. (2006) performed a theoretical study of reflections from the interface between a layer which

55   exhibits fluids-related dispersion and an elastic overburden, and showed that in such cases the AVO response

56   was frequency-dependent. Class I reflections tend to be shifted to higher frequency while class III reflections

57   have their lower frequencies amplified. Recently, the frequency-dependent AVO (FAVO, Wilson et al., 2009;

58   Wilson, 2010) inversion is introduced in an attempt to allow a quantitative measure of dispersion to be derived

59   from pre-stack data. In this paper, we test the FAVO inversion scheme on synthetic and real seismic data to

60   obtain a FAVO attribute. We begin by mathematically formulating the FAVO inversion theory based on Smith

61   and Gidlow's (1987) two-term AVO approximation. Then the resolution of three typical spectral decomposition

62   techniques: the short term Fourier transform (STFT), continuous wavelet transform (CWT) and the smoothed

63   pseudo Wigner-Ville Distribution (SPWVD) based methods, have been discussed. The SPWVD with higher

64   resolution is used to calculate the frequency-dependent spectral amplitudes from pre-stack data. We also discuss

65   the effect of time scale parameter that control the frequency dispersion regime and crack density on the

66   magnitude of dispersion estimation. Finally, the FAVO attribute is applied to seismic data from the North Sea.

67

68   FAVO attribute for seismic dispersion

69   Linear approximations to the exact Zoeppritz reflection coefficients can provide useful insights into subsurface

70   properties. Smith and Gidlow's (1987) removed the density variation ($\Delta\rho/\rho$) from Aki and Richards (1980) by

71   using Gardner et al., (1974) relationship between density and P-wave velocity for water-saturated rocks. Then

72   the approximation becomes two-terms and the P- and S-wave reflectivities ($\Delta V_p/V_p$ and $\Delta V_s/V_s$) can be inverted

73   using parameters that are either known or can be estimated with Least-Square inversion. The reflection

74   coefficient R of Smith and Gidlow's (1987) approximation can be written as:

75
$$R(\theta) \approx A(\theta)\frac{\Delta V_p}{V_p} + B(\theta)\frac{\Delta V_s}{V_s}, \qquad (1)$$

76 where θ is the angle of incidence, the two offset-dependent constants A and B can be derived in terms of V_p, V_s

77 and the angle of incidence (θ_i) which can be calculated by way of ray tracing. Following the theory of Wilson et

78 al.(2010), the coefficients A and B are frequency-independent and do not vary with velocity dispersion, the

79 reflection coefficient R and the P- and S-wave reflectivities $\Delta V_p/V_p$ and $\Delta V_s/V_s$, are considered to vary with

80 frequency due to attenuation and dispersion at the interface or through the hydrocarbon saturated reservoir, then

81 (1) can be written as:

$$R(\theta, f) \approx A(\theta)\frac{\Delta V_p}{V_p}(f) + B(\theta)\frac{\Delta V_s}{V_s}(f) . \qquad (2)$$

83 Expanding (2) as first-order Taylor series around a reference frequency f_0:

$$R(\theta, f) \approx A(\theta)\frac{\Delta V_p}{V_p}(f_0) + (f - f_0)A(\theta)I_a + B(\theta)\frac{\Delta V_s}{V_s}(f_0) + (f - f_0)B(\theta)I_b , \qquad (3)$$

85 where I_a and I_b are the derivatives of P- and S-wave reflectivities with respect to frequency evaluated at f_0:

$$I_a = \frac{d}{df}(\frac{\Delta V_p}{V_p}); I_b = \frac{d}{df}(\frac{\Delta V_s}{V_s}) . \qquad (4)$$

87 For a typical CMP gather with n receivers denoted as a data matrix $s(t, n)$. Coefficients A and B at each sampling

88 point, denoted as $A_n(t)$ and $B_n(t)$, can be derived with the knowledge of velocity model through ray tracing.

89 Spectral decomposition is performed on $s(t, n)$ to derive the spectral amplitude $S(t, n, f)$ at a series of frequencies.

90 However, S contains the overprint of seismic wavelet, so we perform spectral balance, by which the spectral

91 amplitudes at different frequencies are matched to the spectral amplitude at the reference frequency f_0 through a

92 strong continuous reflection caused by elastic interface, to remove this effect with a suitable weight function $w(f,$

93 $n)$:

$$D(t, n, f) = S(t, n, f)w(f, n) . \qquad (5)$$

95   where $D(t, n, f)$ is the balanced spectral amplitude. $w(f, n)$ is calculated from a defined window with k sampling

96   points using the ratio of RMS amplitudes at the chosen reference frequency f_0 and other frequencies as shown in

97   (6),

98
$$w(f,n) = \frac{\sqrt{\sum_k S^2(t,n,f_0)}}{\sqrt{\sum_k S^2(t,n,f)}}$$
(6)

99   Giving the fact that the seismic amplitudes can be associated with the reflection coefficients through convolution

100   with a seismic wavelet in the AVO analysis. The relationship between spectral amplitude and reflectivity

101   depends on the spectral decomposition we used. According to (2), we derive $\Delta V_p/V_p$ and $\Delta V_s/V_s$ at the reference

102   frequency f_0 by replacing R with D. Considering m frequencies $[f_1, f_2, \ldots f_m]$, equation (3) can be expressed as

103   matrix form:

104
$$\begin{bmatrix} D(t,1,f_1) - A_1(t)\dfrac{\Delta V_p}{V_p}(f_0,t) - B_1(t)\dfrac{\Delta V_s}{V_s}(f_0,t) \\ \vdots \\ D(t,1,f_m) - A_1(t)\dfrac{\Delta V_p}{V_p}(f_0,t) - B_1(t)\dfrac{\Delta V_s}{V_s}(f_0,t) \\ \vdots \\ D(t,n,f_1) - A_n(t)\dfrac{\Delta V_p}{V_p}(f_0,t) - B_n(t)\dfrac{\Delta V_s}{V_s}(f_0,t) \\ \vdots \\ D(t,n,f_m) - A_n(t)\dfrac{\Delta V_p}{V_p}(f_0,t) - B_n(t)\dfrac{\Delta V_s}{V_s}(f_0,t) \end{bmatrix} \approx \begin{bmatrix} (f_1 - f_0)A_1(t) & (f_1 - f_0)B_1(t) \\ \vdots & \vdots \\ (f_m - f_0)A_1(t) & (f_m - f_0)B_1(t) \\ \vdots & \vdots \\ (f_1 - f_0)A_n(t) & (f_1 - f_0)B_n(t) \\ \vdots & \vdots \\ (f_m - f_0)A_n(t) & (f_m - f_0)B_n(t) \end{bmatrix} \begin{bmatrix} I_a \\ I_b \end{bmatrix}, (7)$$

105   which can be denoted as:

106
$$RR = RM \begin{bmatrix} I_a \\ I_b \end{bmatrix}.$$
(8)

107   Then the attributes of I_a and I_b can be calculated with least-squares-inversion:

108
$$\begin{bmatrix} I_a \\ I_b \end{bmatrix} = (RM^T RM)^{-1} RM^T RR$$
(9)

109

110

Choice of spectral decomposition techniques

111

112   Application of spectral decomposition techniques allows the frequency-dependent AVO behaviour to be

113   detected from seismic data. A high resolution method is of vital importance for the accuracy and robustness of

114   estimating seismic dispersion. Here we study and compare three different spectral decomposition techniques:

115   short-time Fourier transform (STFT), continuous wavelet transform (CWT) and Wigner-Ville distribution

116   (WVD) based method. The STFT introduced by Gabor (1946) can be expressed as,

117
$$STFT(t,f) = <x(\tau), \varphi(\tau - t)e^{j2\pi f\tau}> = \int_{-\infty}^{\infty} x(\tau)\overline{\varphi}(\tau - t)e^{-j2\pi f\tau}d\tau, \qquad (10)$$

118   where φ is the window function centred at time $\tau = t$, and $\overline{\varphi}$ is the complex conjugate of φ. The STFT is a type

119   of linear Time-Frequency Representation (TFR). The choice of the width of window functions leads to a

120   trade-off between time localization and frequency resolution (Cohen, 1989).

121
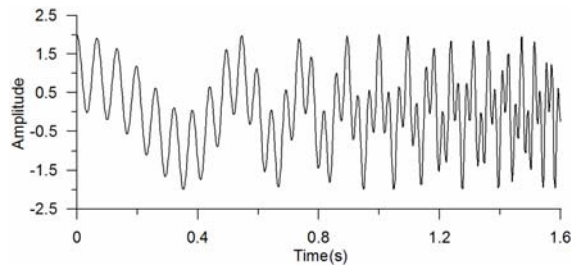
Fig.1 Quadratic FM signal comprised of two frequency components. The frequency of the signal increases
with time.

124   As shown in Fig.1, the signal consists of two quadratic FM signals with different frequency components.

125   The frequency increases with time in quadratic trend, while the amplitude keep unchanged. We use the regularly

126   used window functions: Hamming window, Hanning window, Gauss window and Nuttall window for STFT

127   spectral analysis, for which the expression of window functions are as follows:

128   Hamming window: $w(n) = 0.54 - 0.46 \times \cos(2\pi \frac{n}{N}), \quad 0 \leq n \leq N$;

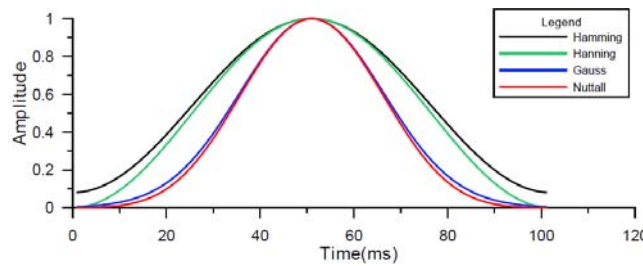129   Hanning window: $w(n) = 0.5(1 - \cos(2\pi \frac{n}{N})), \quad 0 \leq n \leq N$;

130   Gauss window: $w(n) = e^{-\frac{1}{2}\left(\alpha \frac{n}{N/2}\right)^2}$, $-\frac{N}{2} \leq n \leq \frac{N}{2}$, the length of the window is N+1;

131   Nuttall window:

$$w(n) = a_0 - a_1 \times \cos(2\pi\frac{n}{N}) + a_2 \times \cos(4\pi\frac{n}{N}) - a_3 \times \cos(6\pi\frac{n}{N}), \quad 0 \le n \le N$$,

133   where a_0=0.3635819; a_1=0.4891775; a_2=0.1365995; a_3=0.0106411.

134   The shapes of the four window functions are shown in Fig.2. The Hamming window and Hanning window are
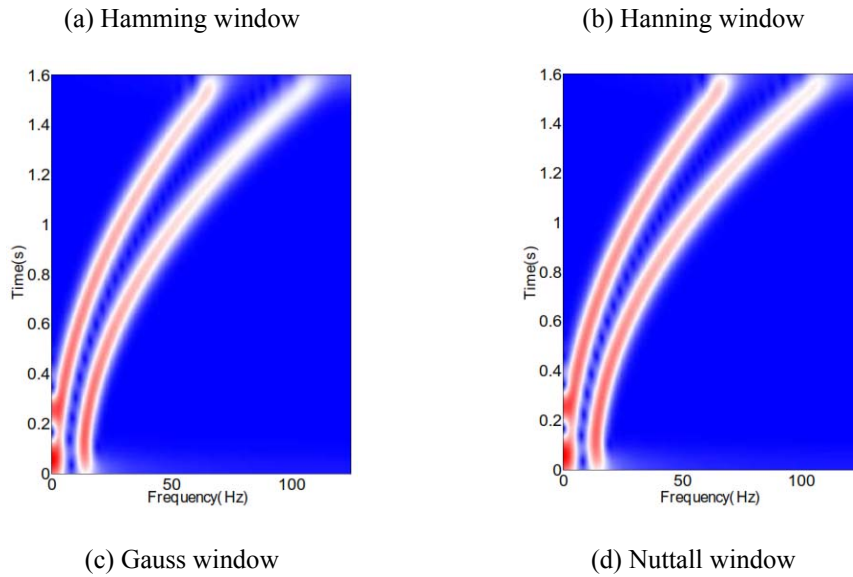
135   wider than the Gauss and Nuttall windows.

Fig.2 The shapes of four different window functions. The Gaussian and Nuttall windows are wider than Hamming and Hanning windows.

139   Fig.3 displays the STFT spectra with the four different window functions. The spectra with the Hamming

140   window and Hanning window have higher frequency resolution especially at low frequencies but low temporal

141   resolution as indicated by the stripes between the two signal components; while the Gauss window and Nuttall

142   window show high temporal resolution especially at high frequency but relatively low frequency resolution at

143   low frequency. However, we can see that Gauss and Nuttall windows provide a better TFR than Hamming and

144   Hanning windows for this signal.

(b) Hanning window

(a) Hamming window   (b) Hanning window

(c) Gauss window   (d) Nuttall window
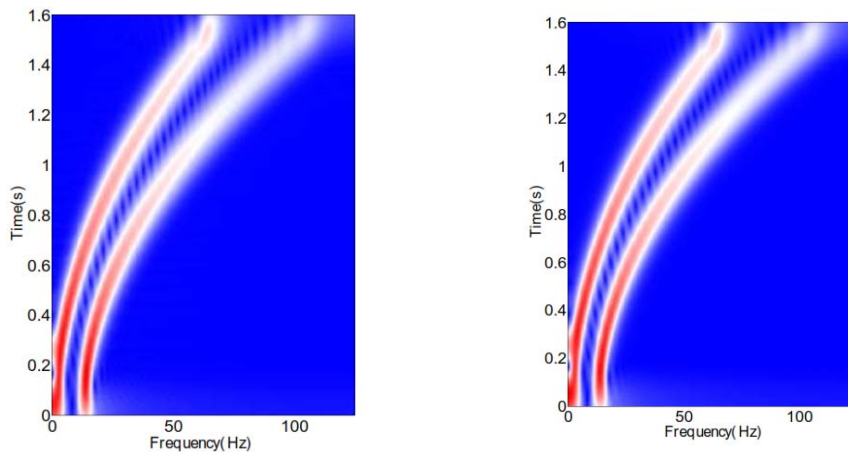
Fig.3 STFT spectra with different window functions. The spectra using Gauss and Nuttall windows have higher temporal resolution than that of using Hamming and Hanning (Windows length: 400ms).

145   The Continuous Wavelet Transform of a signal $s(t)$ is defined as the inner product of a family of

146   wavelets $\psi_{a,b}(t)$ and $s(t)$ (Mallat, 1993, Sinha, et al., 2005):

147
$$S(a,b) =< s(t),\psi_{a,b}(t) >= \frac{1}{\sqrt{|a|}}\int_{-\infty}^{\infty}s(t)\overline{\psi\left(\frac{t-b}{a}\right)}dt \, , \qquad (11)$$

148   where a is the dilation parameter (corresponding to frequency information), b is the translation

149   parameter (corresponding to temporal information), $\overline{\psi(t)}$ is the complex conjugate of $\psi(t)$ 。

150      $S(a,b)$ is the variation of the original signal $s(t)$ with the observation area under different scales at

151   time $t=b$.
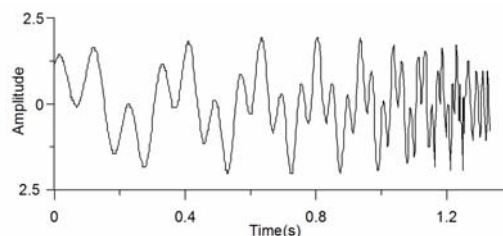
152

153 **Fig.4 Hyperbolic FM signal with two frequency components. The frequency of the signal becomes higher**

154 **with increase of time.**

155   Consider another hyperbolic FM signal with two different frequencies as shown in Fig.4. A 400

156   ms Hamming window is used for STFT and the Morlet wavelet is used for CWT to obtain

157   time-frequency spectra as shown in Fig.5. From Fig.5 (a), we can see STFT spectrum displays high

158   resolution at low frequencies but low resolution at high frequencies due to a predefined window size.

159   Fig.5(b) is the result of CWT, we can see the event is thinner than that of STFT. Frequency resolution

160   at low frequencies is improved. Temporal resolution at high frequency is significantly improved as

161   well due to the dilation of wavelet function.

(a) STFT spectrum   (b) CWT spectrum
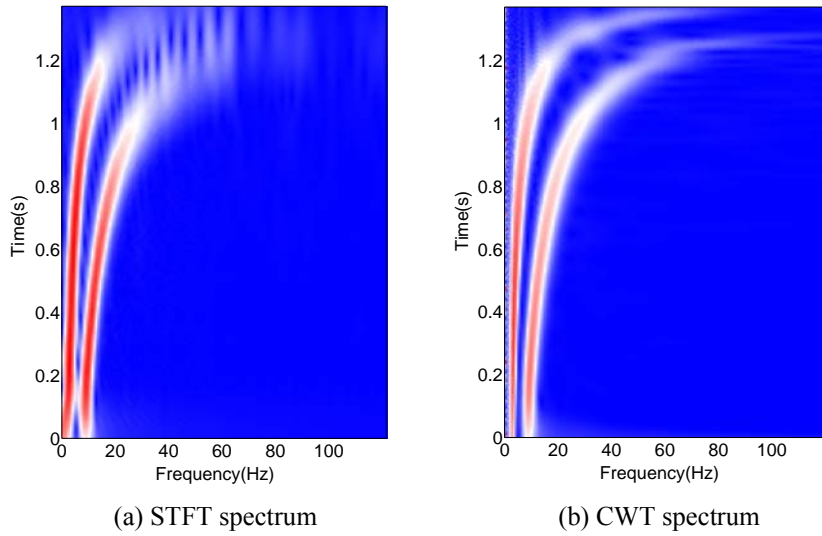
Fig.5 Comparison of STFT and CWT spectra for the FM signal in Fig.4.

162   A third time-frequency representation in seismic signal analysis is the Wigner-Ville distribution

163   (WVD, Classen and Mecklenbräuker, 1980; Cohen, 1989). The WVD of the signal $x(t)$ can be defined

164   as,

$$WVD(t,f) = \int_{-\infty}^{\infty} X(t + \tau/2)\overline{X}(t - \tau/2)e^{-j2\pi f\tau} d\tau \qquad (12)$$

166   Where τ is the time delay variable, $X(t)$ is the analytical signal associated with the real signal $x(t)$,

$$X(t) = x(t) + jH[x(t)] \qquad (13)$$

168    $H[x(t)]$ is the Hilbert transform of $x(t)$ as the imaginary part of $X(t)$. The WVD avoids the STFT

169   trade-off between time and frequency resolution. However, this improvement comes at the cost of the

170   well-known cross-term interference (CTI) caused by WVD bilinear characteristic. One of the

171 improvements is the smoothed pseudo Wigner–Ville distribution (SPWVD), using both a time

172 smoothing window and a frequency smoothing window independently, expressed as

173
$$SW_{g,h,X}(t,f) = \int_{-\infty}^{\infty}\int_{-\infty}^{\infty} X(t+\frac{\tau}{2})\overline{X}(t-\frac{\tau}{2})g(\nu)h(\tau)e^{-j2\pi f\tau}\,d\nu d\tau \qquad (14)$$

174 where ν is the time delay and τ is the frequency offset. $g(\nu)$ is the time smoothing window, $h(\tau)$ the

175 frequency smoothing window on condition that $g(\nu)$ and $h(\tau)$ are both real symmetric functions and

176 $g(0)=h(0)$. Then it is possible to attenuate the CTI presented in the WVD, by independently choosing

177 the type of these two windows.
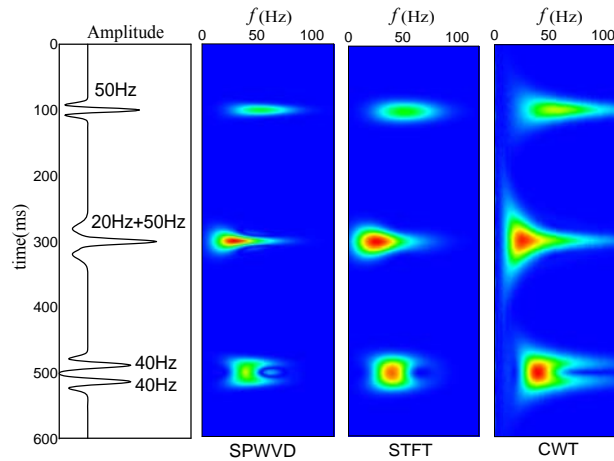
178
179 **Fig.6. A synthetic trace constructed by Ricker wavelets of different centre frequencies and its spectra**
180 **generated with different methods. The SPWVD shows superior resolution than the other methods for this**
181 **signal.**

182   As shown in Fig. 6, a synthetic seismic trace comprised of three components is constructed by

183 adding Ricker wavelets of different centre frequencies. We perform SPWVD with a 30 ms and a 60

184 ms length Gauss low-pass filter as a time and frequency smoothing window, STFT with a 80 ms

185 length Hamming window and CWT with Morlet wavelet. We can see the SPWVD method provides

186 the highest resolution, while both temporal and frequency resolutions are not high enough to

187 demonstrate the spectral characteristics with STFT method. The CWT result shows that the temporal

188 resolution is high but the frequency resolution is low at low frequencies, and the frequency resolution

189   is high but the temporal resolution is low at high frequencies. We use the SPWVD for spectral

190   decomposition of prestack data in the FAVO attribute estimation.

191

192   **Numerical modelling of dispersion estimation**

193   We study a case that considers the effect of variation of timescale τ on the magnitude of dispersion caused

194   by scattering at the interfaces. Timescale τ controls the frequency range over which dispersion occurs. The

195   choice of material parameters is based on the models created by Chapman et al. (2006). The case is a

196   two-layer model, in which the top elastic shale has P- and S-wave velocities of 2743 ms^{-1} and 1394 ms^{-1},

197   and a density of 2.06gcm^{-3}. The lower sandstone is considered to have a P- and S- wave velocities of 2835

198   ms^{-1} and 1472 ms^{-1}, and a density of 2.08gcm^{-3} under water saturation and then change to partial gas

199   saturation with wood equation to calculate the mixed fluid moduli. The parameters of the model are listed

200   in Table 1.

201   Table 1 Material parameters for the two-layer model as described in Chapman et al. (2006).

lithofacies	Vp(ms^{-1})	Vs(ms^{-1})	ρ_W(g.cm^{-3})	ρ_G(g.cm^{-3})	φ(%)	cd(%)	Thickness(m)
Shales	2743	1394	2.06	-	-	-	1000
Sandstone	2835	1472	2.08	2.04	15	5	Half space

202

203   11 receivers were synthesized with a trace spacing of 100 m and 40 Hz Ricker wavelet as the

204   explosive source. Fig.7 displays the four synthetic gathers generated by ANISEIS software package with a

205   Fortran program to create the frequency dependent layer. Two dispersive cases have the same τ value of

206   5×10^{-3} s under water and partial gas saturation respectively. Such a τ value corresponds to the transition

207   frequency being located at the seismic band. The low frequency case ($\tau = 1\times10^{-6}$ s) and the high frequency

208   case (τ = 100 s) have no attenuation and correspond to elastic case. From Fig.7(a), we can see the typical

209   Class I AVO feature that the amplitudes decrease with offset under water saturation. However, Class I

210   AVO changes to Class III AVO when the fluid is substituted with partial gas saturation. Another feature

211   when partial gas saturation is that the amplitudes decrease with increasing τ value. This indicates the

212   reduction of velocity difference and acoustic impedance difference between the two layers from low

213   frequency to high frequency.
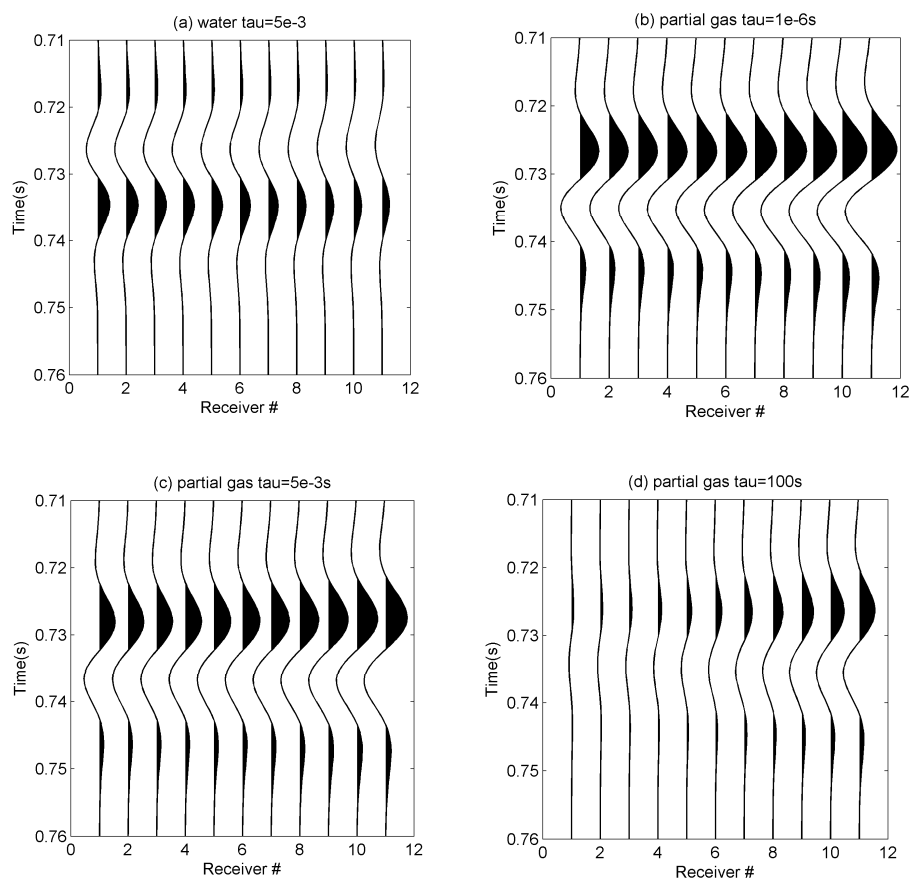
Fig.7 Four synthetic gathers under full water saturation when (a):$\tau = 5\times10^{-3}$s, and partial gas saturation when (b):$\tau = 1\times10^{-6}$s, (c): $\tau = 5\times10^{-3}$s and (d): $\tau = 100$s.

214

215   Using 40Hz (dominant frequency of the source wavelet) as the reference frequency, we calculate the

216   FAVO attribute with the spectral amplitudes at a series of frequencies 25Hz, 30Hz, 40Hz, 50Hz, 60Hz,

217   70Hz and 80Hz. A set of weights were derived in the elastic model by matching the maximum spectral

218   amplitude at non-reference frequencies to the maximum spectral amplitude at 40Hz. These same weights

219   are applied to the dispersive model to remove the wavelet overprint. Since the shear modulus is decoupled

220   from the saturating fluids, we only calculate the derivative of P-wave reflectivity I_a. Fig.8 displays a

221   comparison between the balanced isofrequency sections at 25Hz, 50Hz and 80Hz for the two dispersive

222   models under water and partial gas saturation respectively. We can see that for partial gas, energy decreases

223   with increasing frequency, whereas energy increases with increasing frequency when saturated with water.

(a) water saturation

(b) partial gas saturation
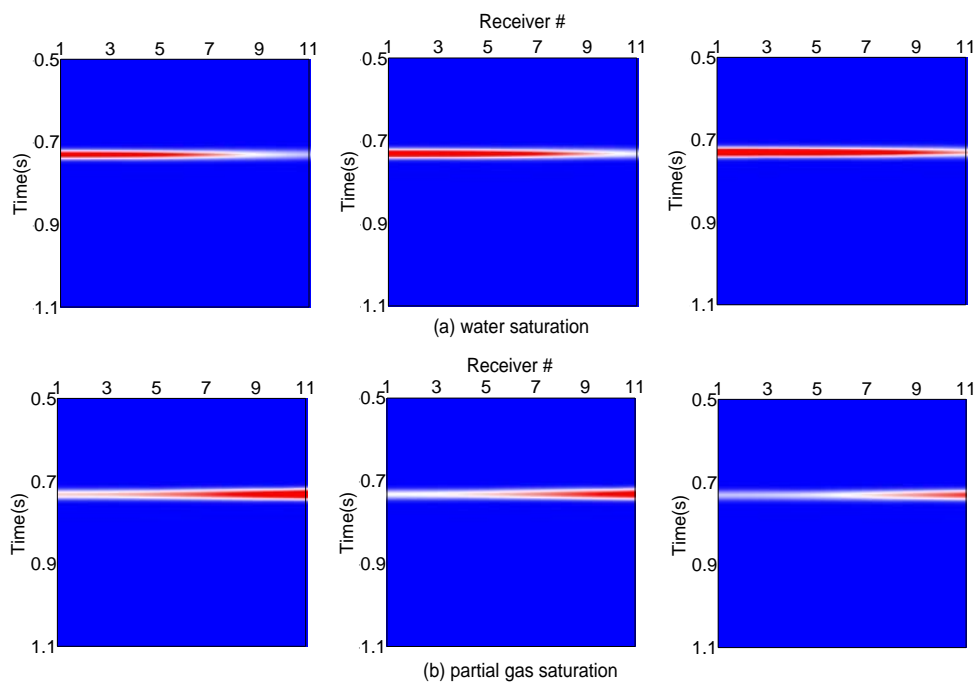
224

225   **Fig.8 Isofrequency sections at 25Hz, 50Hz and 80Hz for the dispersive models under water and partial gas**
226   **saturation respectively ($\tau = 5\times10^{-3}$s).**

227   Fig.9 displays the I_a attribute for the four models. We can see that the magnitude of P-wave dispersion

228   for the partial gas saturation when $\tau = 5\times10^{-3}$s (c) is the highest. This is much more significant than low and

229   high frequency cases (b and d), of which there is almost no dispersion occurring. The result for dispersive

230   model under water saturation (a) is a little weak compared with (c), indicating the magnitude of dispersion

231   is weaker than partial gas saturation. This can be seen from the isofrequency sections.
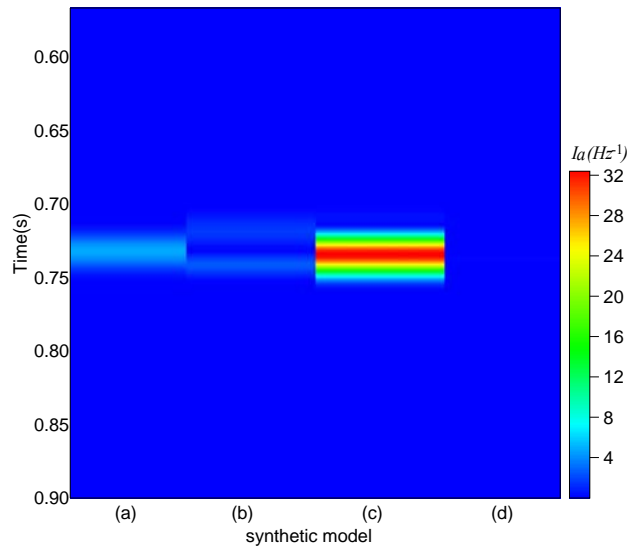
Fig.9 The attribute of derivative of P-wave reflectivity I_a for the four synthetics models as displayed in Fig.7.

Fig.10 displays the reflection coefficients varying with angle of incidence at frequencies 25, 30, 40, 50, 60, 70 and 80Hz under the two dispersive models (Fig.7 a and c). Comparing the amount of separation between the curves of different frequencies, we can see that there is stronger dispersion within the seismic bandwidth in the synthetic seismogram under partial gas saturation. This is corresponds to the result displayed in Fig.9.

(a)

(b)
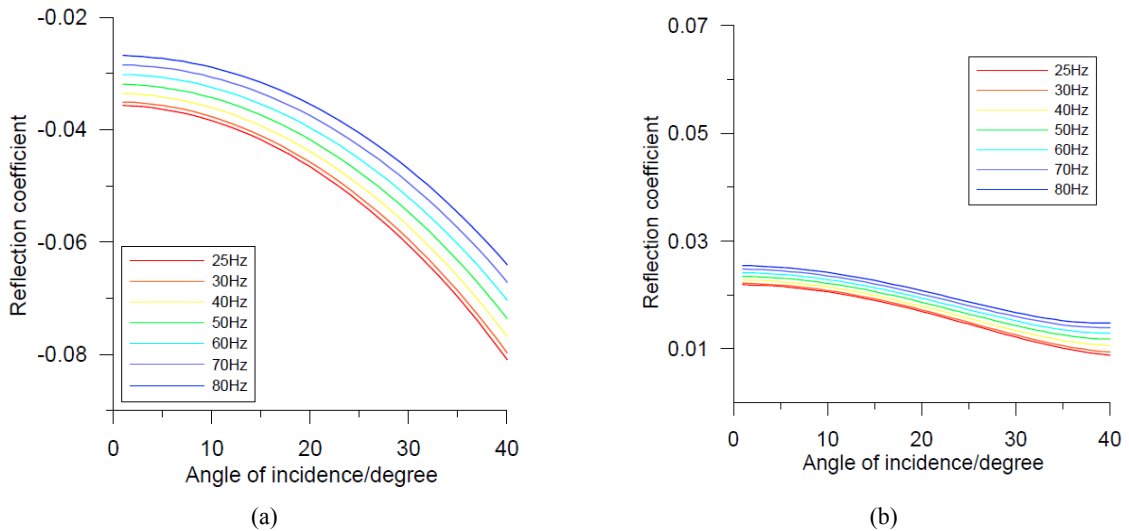
Fig.10 The P-wave reflection coefficient versus angle of incidence for the two dispersive model under water and partial gas saturation respectively.(a)partial gas saturation;(b)water saturation.

241   In the second case we create a three-layer model with varying crack densities of 5%, 10%, 15% and 20%

242   for the dispersive sandstone under gas saturation, in order to study the influence of crack density on the

243   magnitude of dispersion. The P-wave and S-wave velocity and density are the same as that of the previous

244   example, but an elastic overburden shale layer is added to form an elastic interface for spectral balance. All

245   the parameters are listed in Table 2. Using 40Hz Ricker wavelet as the source, we create the four models

246   with 4 receivers (1.1km – 1.4km) at a trace spacing of 100m. Fig.11 displays the synthetic seismograms

247   when varying crack densities. It is clear that reflection amplitude from the second interface increase with

248   increasing crack density.

249   Table 2 Material parameters for the three-layer model as described in Chapman et al. (2006).

| lithofacies	Vp(ms^{-1})	Vs(ms^{-1})	ρ_W(g.cm^{-3})	ρ_G(g.cm^{-3})	φ(%)	cd(%)	Thickness(m)
Shales	2500	1250	2.02	-	-	-	1000
Shales	2743	1394	2.06	-	-	-	300
Sandstone	2835	1472	2.08	2.04	15	5,10,15,20	Half space
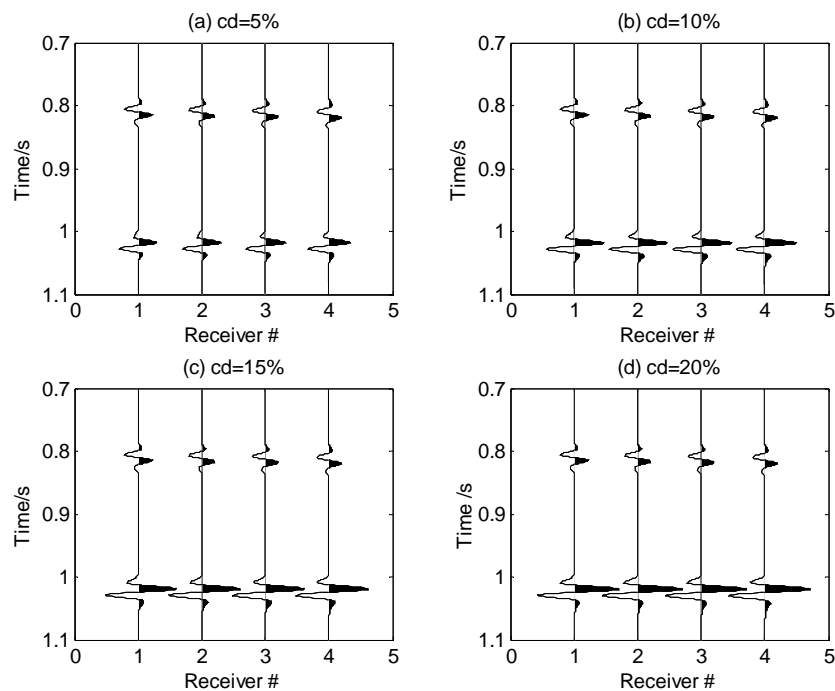
250

251   **Fig.11 Three-layer model with different crack densities.**

252　　Using the same set of frequencies at 25Hz, 30Hz, 40Hz, 50Hz, 60Hz, 70Hz, 80Hz and 40Hz as reference

253　　frequency for spectral balance, we implement FAVO attribute and obtain the I_a of the four models as

254　　shown in Fig.12. We can find that there is no dispersion for the first interface at 0.8s, whereas there is

255　　conspicuous dispersion for the second interfaces at 1.02s. The I_a value increases as crack density increases.
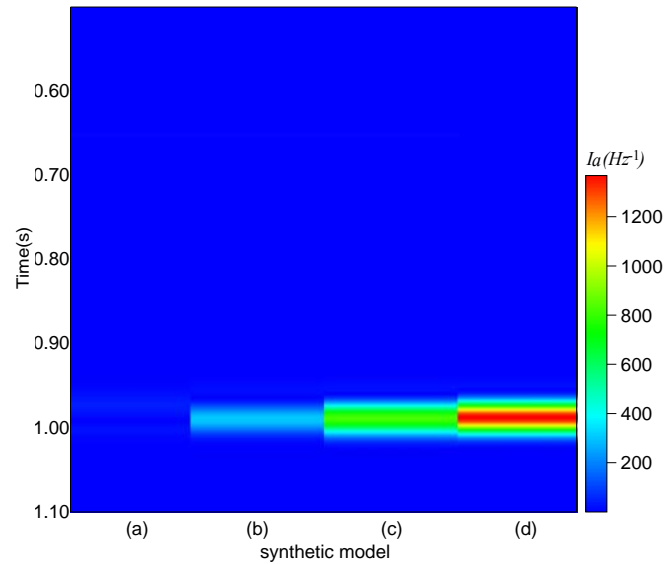

256

257　**Fig.12 The derivative of P-wave reflectivity *Ia* under different crack densities for the four synthetics**
258　**models as displayed in Fig.11.**

259

Cases study

261　　Numerical test has demonstrated that the FAVO attribute scheme is able to quantitatively estimate seismic

262　　dispersion and separate dispersive models from elastic models. In this section, we present the application of

263　　FAVO attribute to real seismic data from the North Sea. Selection of optimal frequencies and reference

264　　frequency for spectral decomposition is a key issue for the calculation of FAVO attribute. To this end, we

265　　analyze the energy distribution an arbitrary pre-stack trace with Fast Fourier Transform (FFT). As shown in

266　　Fig.13, the dominant frequency is around 15Hz with bandwidth from 0Hz to 40Hz for prestack trace. We

267　　define the reference frequency $f_{ref} = 15$Hz and select a set of frequencies at 10Hz, 15Hz, 20Hz, 30Hz, 40Hz

268　　for the FAVO attribute.
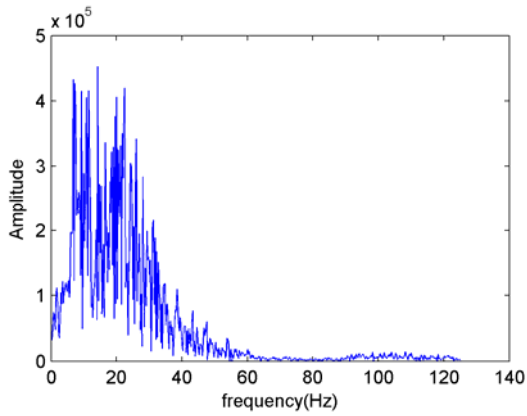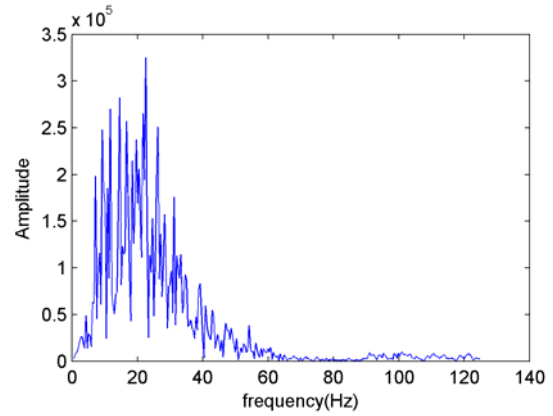
pre-stack trace   stacked trace

**Fig.13 Spectral analysis of a arbitrary prestack trace.(a)the whole trace (b)trace under 1.6s.**

269 Fig.14 (a) displays the stacked section of Xline4921 from the North Sea. The target is around 2.0s,

270 corresponding to a relatively deep depth of about 2km. The positions of potential reservoir exhibit as

271 "bright spots", where the pre-stack CMP gathers have the feature of Class III AVO. We perform SPWVD

272 on the stacked section to obtain isofrequency sections at 10Hz, 15Hz, 20Hz, 30Hz, and 40Hz. Continuous

273 reflections above1.0s can be deemed to be caused by elastic interface, therefore can be used for spectral

274 balance with 15Hz as reference frequency. Fig.14 (b-f) display the balanced isofrequency section at 10Hz,

275 15Hz, 20Hz, 30Hz, 40Hz of the stacked section. We can see that spectral amplitudes at left and middle

276 anomalies have a trend of increasing with frequency, whilst spectral amplitudes at the right anomaly is

277 stable at 10Hz, 15Hz, 20Hz and then decrease at 30Hz and 40Hz.
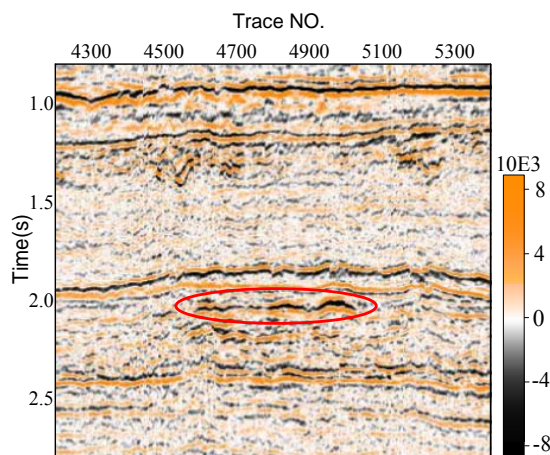
(a) Stacked section of Xline4921   (b) 10Hz

(c) 15Hz   (d) 20Hz
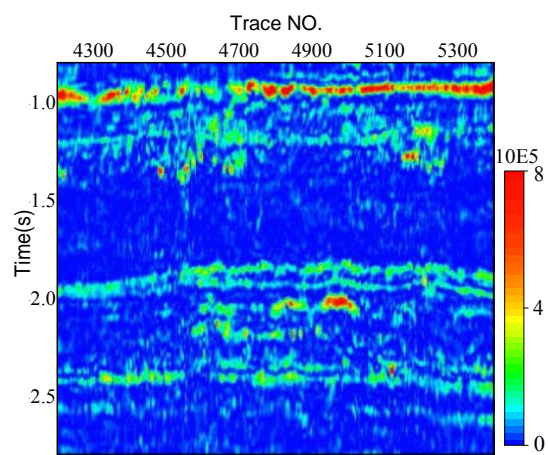
(e) 30Hz   (f) 40Hz
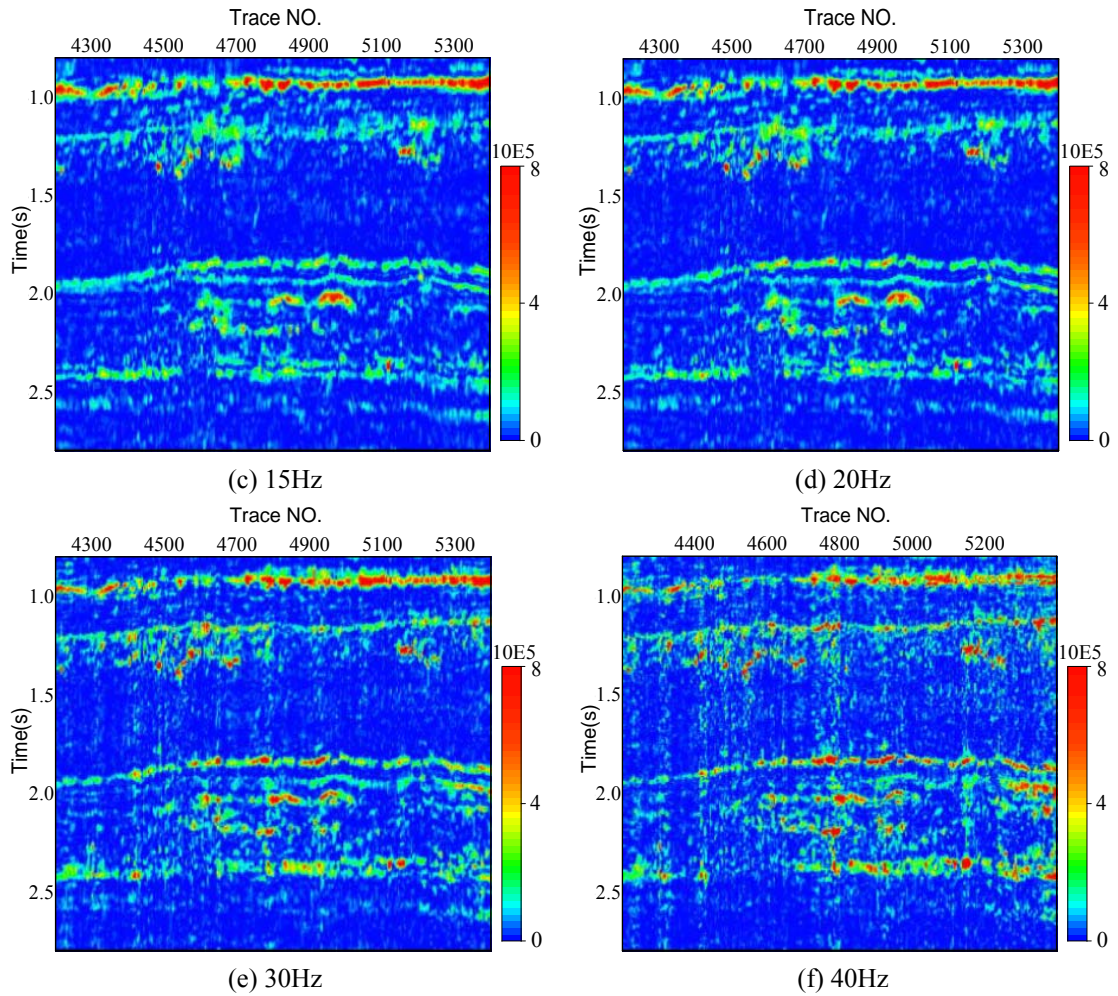
Fig.14 The Stacked section of Xline4921 and its isofrequency sections.

278

279   The pre-stack CMP gathers from No.4201 to No.5399 are extracted from the 3D seismic data for the

280   calculation of I_a attribute. In order to reduce the influence of NMO stretching, we use the first 45 traces for

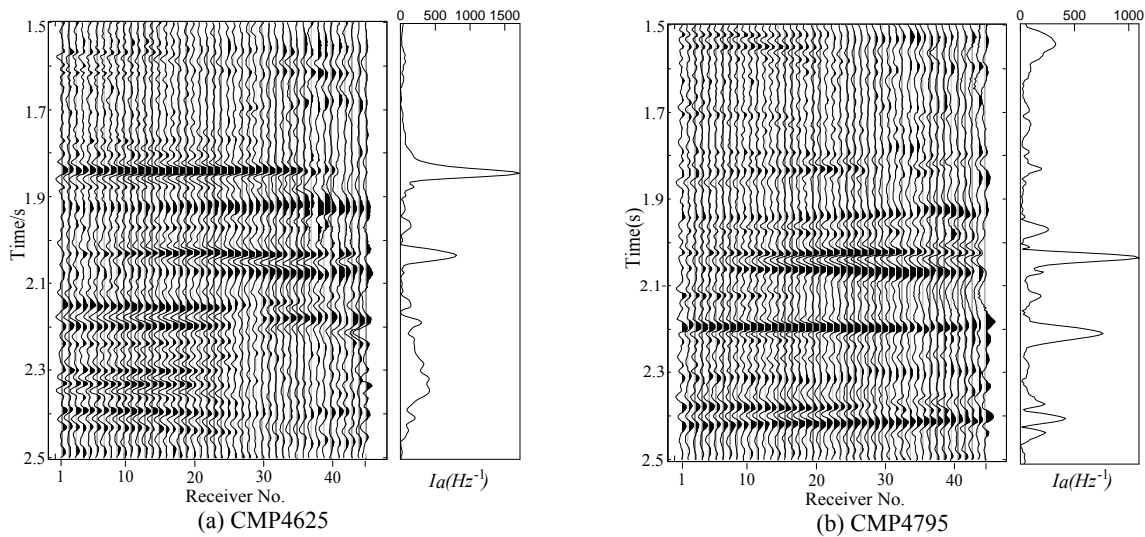281   the FAVO attribute.

282

283   We perform the SPWVD on each pre-stack gather to obtain isofrequency sections at 10, 15, 20, 30 and

284   40Hz. A trace of I_a attribute can be calculated for each pre-stack gather. Figure 15 displays the I_a attribute

285   for the CMP numbers from 4201 to 5399. We can see strong reflection energy due to non-reservoir

286   interfaces in Figure 14 has been partially eliminated in this attribute. The zone of interest around 2.0s

287   shows significant magnitude of dispersion. Figure 16 displays the No.4625 and No.4795 CMP gather. The

288   amplitudes exhibit the typical feature of Class III AVO at the reservoir position. The inverted I_a attribute on

289   the right shows maximum amplitude around this area, which may caused by fluids saturation.

290
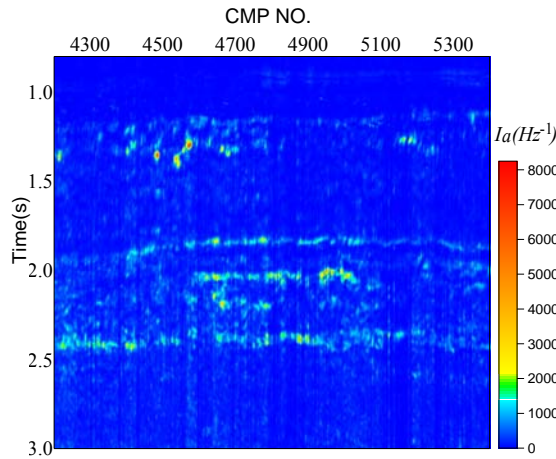
291   **Fig.15 The I_a attribute for the CMP number from 4201 to 5399.**

292

(a) CMP4625   (b) CMP4795

            Fig.16 The calculated I_a attribute for the two CMP gathers.

293

Conclusions

295   In this paper, we have developed a FAVO attribute to demonstrate the possibility of inferring dispersion

296   properties directly from pre-stack data and linking this to fluid saturation. The attribute combines a

297   high-resolution spectral decomposition technique with Smith and Gidlow (1987)'s AVO approximation. We

298 illustrate the method through analysis of synthetic data. The real seismic example from the North Sea indicates

299 the potential of this method for the detection of seismic dispersion resulting from fluid saturation.

300 We also compare three typical spectral decomposition techniques and use SPWVD in the FAVO attribute.

301 forward modelling indicates that the FAVO attribute can determine the maximum magnitude of P-wave

302 dispersion for dispersive partial gas saturation case. Higher crack density gives rise to stronger magnitude of

303 P-wave dispersion. Real seismic data example from the North Sea suggests the potential of this method for

304 detection of seismic dispersion due to fluid saturation.

305 It is worth to mention that the inversion scheme still may be affected by NMO stretching. For deep reservoirs,

306 we use near-offset traces only in order to reduce the affect of NMO stretching, but for shallow reservoirs the

307 NMO stretching should be corrected before inversion.

308

313

314 **References**

315 Aki, K. and Richards, P.G., 1980. Quantitative Seismology. W.H. Freeman and Co.

316 Bath M．Spectral Analysis in Geophysics．New York：Elsevier，1974．

317 Castagna, J.P., Sun, S. and Siegfried, R.W., 2003. Instantaneous spectral analysis: detection of
318 low-frequency shadows associated with hydrocarbons, The Leading Edge, 22(3): 120-127.

319 Chapman, M., 2003. Frequency dependent anisotropy due to meso-scale fractures in the presence of equant
320 porosity, Geophys. Prospect., 51, 369–379.

321 Chapman, M., Liu, E., and Li, Xiang-Yang, 2006, The influence of fluid-sensitive dispersion and
322 attenuation on AVO analysis, Geophysical Journal International, 167, 89-105.

323   Claasen, T., Mecklenbräuker, W., 1980. The Wigner distribution: a tool for time - frequency signal
324   analysis. Philips Journal of Research 35, 217-250.

325   Cohen, L., 1995. Time–Frequency Analysis. Prentice Hall Inc., New York, USA.

326   Dasgupta, R., and Clark, R.A., 1998, Estimation of Q from surface seismic reflection data: Geophysics, 63,
327   2120-2128.

328   Gabor, D., 1946, Theory of communication. J.IEE, 93:429-457.

329   Gardner, G.H.F., Gardner, G.L. and Gregory, A.R., 1974. Formation velocity and density – The diagnostic
330   basics for stratigraphic traps. Geophysics, 39, 770-780.

331   Gist, G. A., 1994. Interpreting laboratory velocity measurements in partially gas-saturated rocks:
332   Geophysics, 59, 1100–1109.

333   Gurevich, B., Makarynska, D., de Paula, O., & Pervukhina, M., 2010. A simple model for squirt-flow
334   dispersion and attenuation in fluid-saturated granular rocks. Geophysics. 75 (6): pp.N109-N120.

335   Hauge P. S., 1981. Measurements of attenuation from vertical seismic profiles. Geophysics, 46, 1548 -
336   1558.

337   Mallat, S.G.,1999, A wavelet tour of signal processing. Academic Press.

338   Müller T. M., & E. Rothert, 2006. Seismic attenuation due to wave-induced flow: Why Q in random
339   structures scales differently, Geophysical Research Letters, VOL. 33, L16305.

340   Murphy, W.F., 1982. Effects of partial water saturation on attenuation in massilon sandstone and vycor
341   porous glass, Acoust. Soc. Am. J., 71, 1458–1468.

342   Quan, Y. & Harris, J. M., 1997. Seismic attenuation tomography using the frequency shift method.
343   Geophysics, 62(3), 895 - 905.

344   Quintal, B. & Tisato, N., 2013. Modeling Seismic Attenuation Due to Wave-Induced Fluid Flow in the
345   Mesoscopic Scale to Interpret Laboratory Measurements. Fifth Biot Conference on Poromechanics, Vienna,
346   pp. 31-40.

347   Sinha, S., Routh, P.S., Anno, P.D., Castagna, J.P., 2005. Spectral decomposition of seismic data with
348   continuous wavelet transform. Geophysics 70 (6), 19–25.

349   Smith, G.C., and Gidlow, P.M., 1987. Weighted stacking for rock property estimation and detection of gas:
350   Geophysical Prospecting, 35, 993-1014.

351   Taner, M.T., and Treitel, S., 2003, A robust method for Q estimation: 73rd Annual SEG Meeting Expanded
352   Abstracts, 710-713.

353   Tonn, R., 1991, The determination of seismic quality factor Q from VSP data: A comparison of different
354   computational methods: Geophys. Prosp., 39, 1-27.

355　White, J. E., 1975. Computed seismic speeds and attenuation in rocks with partial gas saturation,
356　Geophysics, 40, 224-232.

357　Wilson A., Chapman M., and Li X-Y., 2009. Frequency-dependent AVO inversion, 79th annual SEG
358　meeting Expanded Abstracts, 28, 341-345.

359　Wilson A., 2010.Theory and Methods of Frequency-Dependent AVO Inversion. PhD Thesis, University of
360　Edinburgh.

361　Wu X., and Liu T., 2009. Spectral decomposition of seismic data with reassigned smoothed pseudo
362　Wigner-Ville distribution, Journal of Applied Geophysics, 68(3): 386-393.

363　Wu, X., Chapman, M., and Li, X-Y., 2010. Estimating seismic dispersion from pre-stack data using
364　frequency-dependent AVO inversion. 80th annual SEG meeting Expanded Abstracts, 29, 341-345.